

SwarmDiffusion: End-To-End Traversability-Guided Diffusion for Embodiment-Agnostic Navigation of Heterogeneous Robots

Iana Zhura, Sausar Karaf, Faryal Batool, Nipun Dhananjaya Weerakkodi Mudalige, Valerii Serpiva, Ali Alridha Abdulkarim, Aleksey Fedoseev, Didar Seyidov, Amjad Hajira, Dzmitry Tsetserukou

Abstract—Visual traversability estimation is critical for autonomous navigation, but existing VLM-based methods rely on hand-crafted prompts, generalize poorly across embodiments, and output only traversability maps, leaving trajectory generation to slow external planners.

We propose SwarmDiffusion, a lightweight end-to-end diffusion model that jointly predicts traversability and generates a feasible trajectory from a single RGB image. To remove the need for annotated or planner-produced paths, we introduce a planner-free trajectory construction pipeline based on randomized waypoint sampling, Bézier smoothing, and regularization enforcing connectivity, safety, directionality, and path thinness. This enables learning stable motion priors without demonstrations.

SwarmDiffusion leverages VLM-derived supervision without prompt engineering and conditions the diffusion process on a compact embodiment state, producing physically consistent, traversable paths that transfer across different robot platforms.

Across indoor environments and two embodiments (quadruped and aerial), the method achieves 80–100% navigation success and 0.09 s inference, and adapts to a new robot using only 500 additional visual samples. It generalizes reliably to unseen environments in simulation and real-world trials, offering a scalable, prompt-free approach to unified traversability reasoning and trajectory generation.

Index Terms—Foundation Models, Traversability Estimation, Embodiment Agnostic Navigation

I. INTRODUCTION

RELIABLE indoor navigation is fundamental to a wide range of robotic applications, including warehouse automation [1], industrial inspection [2], search and rescue, and autonomous logistics. In these settings, robots must continuously reason about where they can safely move and how to plan a feasible trajectory through cluttered, unstructured, and dynamic spaces. Accurate traversability estimation and trajectory generation predicting whether a region is safe to traverse and computing a collision-free path through it are central to safe and reliable robot autonomy.

Classical geometric pipelines estimate traversability from depth or occupancy maps and depend heavily on precise metric maps, careful tuning, and strong initialization. This makes them brittle in indoor environments with irregular geometry, reflective surfaces, and occlusions. Recent self-supervised learning methods [3], [4] overcome some of these limitations by inferring traversability directly from visual perception. Yet, such models must be retrained for every new

The authors are with the Intelligent Space Robotics Laboratory, Center for Digital Engineering, Skolkovo Institute of Science and Technology. {iana.zhura, sausar.karaf, faryal.batool, nipun.weerakkodi, valerii.serpiva, ali.abdulkarim, aleksey.fedoseev, didar.seyidov, hajira.amjad@skoltech.ru, d.tsetserukou}@skoltech.ru

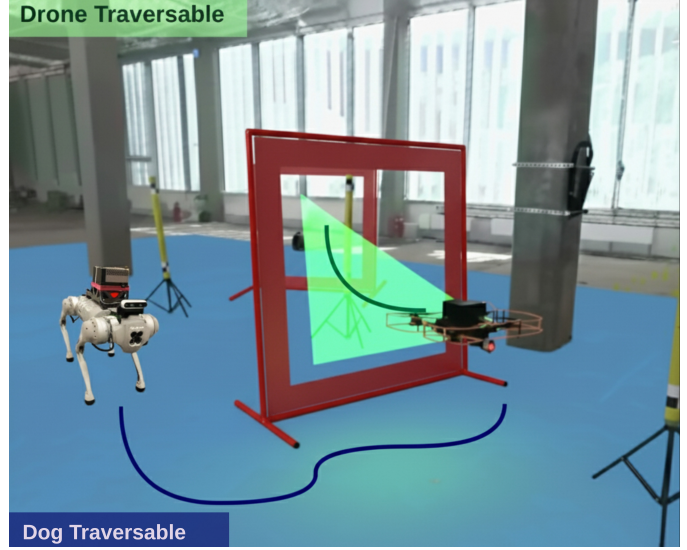


Fig. 1. Cross-embodiment traversability transfer and feasible trajectory generation. The legged robot (source) explores the environment and builds a traversability prior (blue path), which the aerial robot (target) uses for safe navigation through the shared workspace (green volume).

robot embodiment because they rely on the sensor-specific supervision signal, constraining their generalization to unseen platforms and environments.

Large vision–language models (LVLMs) have recently been explored for prompt-driven indoor navigation and traversability reasoning [5], [6]. While promising, their output quality depends heavily on prompt wording and scene descriptions, and they fail to deliver pixel-accurate or physically feasible trajectories without additional planning or manual intervention. Moreover, their reliability deteriorates for uncommon viewpoints such as those of aerial robots or in scenes with visual ambiguity, clutter, or poor lighting.

In contrast, our goal is to enable robots to directly infer *both* traversable regions and a feasible long-horizon trajectory from a single RGB image, without relying on expert demonstrations, explicit 3D mapping, or human-provided prompts. Such a capability is especially important indoors, where narrow corridors, dense obstacles, and high structural variability make accurate trajectory prediction indispensable for safe operation.

To this end, we introduce a single conditional diffusion model that jointly generates a traversability map and a feasible trajectory only from an RGB image and a robot state vector. The model is trained without expert trajectories and operates purely in 2D image space, allowing it to generalize across heterogeneous embodiments such as legged and aerial robots.

By learning an implicit representation of scene structure and motion feasibility, it produces globally coherent and semantically consistent trajectories that follow traversable regions in the environment.

Since trajectory generation occurs in image space, projecting the resulting path into 3D introduces mild geometric uncertainty, especially for aerial viewpoints or long-range planning. To ensure safety during real-world deployment, we incorporate a lightweight Artificial Potential Field (APF) refinement that uses point-cloud distances to perform small, local corrective adjustments. This refinement acts solely as a safety layer, *not* a planner, adds negligible latency, and requires neither intermediate mapping nor re-running the diffusion inference. Overall, our goal is to enable scalable, prompt-free, cross-embodiment navigation by learning a shared visual traversability representation that supports both global planning and local collision avoidance.

Contributions

This work makes the following contributions:

- 1) **Unified end-to-end generative navigation.** We propose the first diffusion-based framework that jointly generates traversability maps and feasible trajectories from a single RGB image, start, and goal. The model functions as both a global and local planner and requires *no* expert demonstrations.
- 2) **Embodiment-agnostic planning across robots.** Operating entirely in 2D image space enables the same model to be deployed on heterogeneous embodiments (legged and aerial) without retraining or prompt engineering.
- 3) **Lightweight 3D safety refinement.** A minimal APF-based correction uses point-cloud distances to compensate for image-to-3D projection errors, adding negligible latency and avoiding re-mapping or re-planning.
- 4) **Robustness beyond classical optimization.** By implicitly encoding scene structure and traversability, our diffusion model provides a globally coherent initialization that overcomes common failure modes of classical optimizers and APF-only planners.
- 5) **Real-world and simulation validation.** We demonstrate successful deployment on a Unitree Go1 quadruped and a custom-built drone, alongside a high-fidelity Unity-based simulation. A full ROS 2 implementation and training pipeline will be released publicly.

II. RELATED WORK

A. Self-Supervised Traversability Estimation

Self-supervised traversability estimation typically derives supervision from a robot’s own interactions and later regresses it from visual perception. Early methods operate on RGB inputs [3], [7], [8], while others incorporate LiDAR or depth [9]–[11]. Supervisory signals have been extracted from acoustic feedback [12], wheel–terrain interaction, or discrepancies between commanded and executed velocities [3]. Frameworks such as BADGR [8] jointly predict collision risk and vibration magnitude, and WVN [3] incorporates human preference learning.

Despite their success, these approaches require robots to physically experience diverse terrain types for long durations, making them strongly embodiment- and environment-dependent and limiting rapid deployment in unseen indoor settings. To reduce reliance on robot interaction, VLM-based approaches such as AnyTraverse [5] infer traversability directly from RGB images via human-written prompts, enabling generalization but remaining sensitive to prompt quality and largely agnostic to embodiment constraints. SALON [13] mitigates prompt dependence through coarse human initialization followed by self-improvement, yet still requires substantial online exploration.

Overall, self-supervised and VLM-based methods either demand extensive robot–environment interaction, depend heavily on prompt wording, or lack embodiment-aware feasibility reasoning, and none jointly predict traversability and a physically plausible trajectory within a single unified model operable across heterogeneous platforms.

B. Path Optimization and Visual Navigation

Path planning and visual navigation have long been central problems in robotics. Existing approaches include classical vision-based pipelines, reinforcement learning, and recent generative models, yet all typically separate perception from planning and depend on costmaps or handcrafted priors.

1) *Classical vision-based navigation and optimization-based planning:* Classical pipelines typically involve perception, mapping, costmap generation, and trajectory optimization. Ran et al. [14] used CNN-based scene classification for indoor navigation, while Wang et al. [15] developed object-based topological mapping with graph search. However, these methods rely on hand-crafted cost functions and explicit map construction, which limits their robustness in cluttered indoor spaces. Optimization-based planners such as CHOMP, TrajOpt, and NLP solvers require precise metric maps, strong initialization, and incur high computational cost, making them brittle in visually ambiguous or partially observable environments.

2) *Reinforcement Learning approaches:* Reinforcement learning has been widely applied to navigation, including DRL-based collision avoidance [16], UAV path planning via region segmentation and reward shaping [17], safety-constrained RL (SafeMove-RL) [18], and model-based RL for agile flight [19]. RL methods offer adaptability but typically require extensive training, exhibit poor cross-embodiment generalization, and remain sensitive to task-specific reward design and environmental variation.

3) *Diffusion-based and VLM-based motion planning:* Diffusion models have recently been applied to motion generation, including quadruped pose diffusion (DiPPEST) [20], goal-conditioned exploration (NoMaD) [21], cost-aware trajectory generation (MPD) [22], and diffusion-based navigation from images (VENTURA [23], NaviDiffusor [24]). Other work investigates diffusion for FPV video synthesis [25]. While effective, these methods generally rely on precomputed costmaps or external traversability estimates, do not jointly infer traversability and trajectories, and often require explicit geometric reasoning or optimization at deployment.

For UAVs, safety-focused navigation methods such as GPS-denied collision avoidance [26] and EAST [27] provide guarantees via handcrafted constraints or barrier functions, but still depend on modular perception–planning pipelines.

4) *Multi-agent navigation and cooperative planning:*

Multi-agent navigation highlights further limitations of modular learning pipelines. Decentralized collision avoidance [16], NeuroSwarm’s aerial–ground mapping and planning framework [28], heterogeneous MARL for search-and-rescue [29], and game-theoretic UAV coordination [30] all rely on explicit communication, handcrafted structures, or separate perception and planning modules, and none achieve end-to-end traversability and trajectory inference from a single first-person image.

Across classical, RL-based, diffusion-based, and multi-agent systems, current approaches depend on explicit costmaps, handcrafted constraints, or extensive interaction data and separate mapping–planning modules; critically, none jointly estimate traversability and generate a feasible trajectory in a single, low-latency model that generalizes across heterogeneous robots. This gap motivates our unified diffusion framework, which directly produces traversability maps and trajectories from visual input without expert demonstrations, prompt engineering, or explicit optimization.

III. PROBLEM FORMULATION

We consider heterogeneous robotic platforms: specifically a quadruped and an aerial robot, each with embodiment-specific locomotion and safety constraints. At time t , the robot receives a frontal RGB image:

$$I_t \in \mathbb{R}^{H \times W \times 3}, \quad (1)$$

along with its proprioceptive state:

$$s_t = (x_t, y_t, z_t, \phi_t, \theta_t, \psi_t) \in \mathbb{R}^6, \quad (2)$$

and embodiment type e_t .

a) *Traversability field:* We model the environment through an unknown traversability function:

$$T_t : \Omega \rightarrow [0, 1], \quad \Omega = \{1, \dots, H'\} \times \{1, \dots, W'\}, \quad (3)$$

where $T_t(u, v) = 1$ denotes fully traversable terrain and $T_t(u, v) = 0$ indicates unsafe or obstacle regions. Since T_t is unobservable, the robot must infer a traversability estimate from visual and state inputs. We denote the model-predicted traversability map by:

$$\hat{T}_t = f_\theta^{\text{trav}}(I_t, s_t, e_t). \quad (4)$$

b) *Trajectory:* The goal is to generate a discrete trajectory in image-plane coordinates:

$$\tau = (p_0, p_1, \dots, p_K), \quad p_k \in \Omega, \quad (5)$$

connecting a specified start and goal location encoded as a two-channel start–goal tensor:

$$S_t \in \mathbb{R}^{2 \times H' \times W'}. \quad (6)$$

c) *Embodiment-feasible motion set:* Because different embodiments admit different admissible motions, we define

$$\mathcal{A}(e_t, s_t), \quad (7)$$

as the set of feasible trajectories for the embodiment e_t under state s_t .

d) *Objective.:* We seek a mapping

$$F : (I_t, s_t, e_t, S_t) \longrightarrow (\hat{T}_t, \tau), \quad (8)$$

that simultaneously predicts the traversability map \hat{T}_t and a feasible trajectory $\tau = (p_0, \dots, p_K)$ satisfying the following:

(Connectivity)

$$p_0 = p_{\text{start}}, \quad p_K = p_{\text{goal}}, \quad (9a)$$

(Safety)

$$\hat{T}_t(p_k) \geq \delta, \quad \forall k = 0, \dots, K, \quad (9b)$$

(Embodiment-Feasibility)

$$\tau \in \mathcal{A}(e_t, s_t), \quad (9c)$$

(Cross-Embodiment Transfer)

$$F(I_t, s_t, e_{\text{tgt}}, S_t) \approx F(I_t, s_t, e_{\text{src}}, S_t), \quad (9d)$$

ensuring that trajectory generation remains consistent across embodiments, despite differing dynamics, viewpoints, and traversability constraints.

e) *Joint traversability and trajectory learning:* A key requirement of our formulation is that the *same model* learns both: (i) to predict the traversability field \hat{T}_t , and (ii) to generate a feasible trajectory τ conditioned on it.

IV. TECHNICAL APPROACH

A. Network Architecture

In this section, we present the methodology of our proposed framework, which first identifies the platform-specific traversability region of interest and initializes a random trajectory sample within the most traversable areas. Noise is then injected into this trajectory, and the model learns to predict (and remove) this noise while being conditioned on both the traversability map and the encoded embodiment state vector. Through this process, the model simultaneously learns embodiment-specific traversability estimation and trajectory denoising, enabling it to generate feasible paths tailored to the robot’s dynamics and environmental constraints.

1) *Trajectory heatmap generation:* To supervise trajectory denoising, we synthetically generate compact trajectory heatmaps for each scene. A small set of waypoints is sampled using Gaussian perturbations and interpolated with a Bézier curve for smoothness. The curve is densified, rasterized onto a 64×64 grid, and rendered as a thin trace using one-pixel discs followed by a light Gaussian blur. The resulting heatmap is normalized to $[0, 1]$, providing a consistent supervision target that encodes smooth, connected motion patterns aligned with the scene geometry.

2) *Traversability teacher model*: Reliable traversability supervision is obtained from the AnyTraverse teacher model [5], which generates platform-specific traversability maps and regions of interest. These teacher outputs provide (i) ground-truth signals for training the student traversability module and (ii) conditioning inputs for the diffusion model to guide trajectory generation toward safe, feasible areas. To enable prompt-free deployment, we additionally train a traversability prediction module that reconstructs platform-specific traversability directly from visual inputs, removing the need for external prompts or intermediate mapping at inference time.

3) *Traversability student model*: The traversability student model employs a frozen DINO-v2 ViT backbone [31] with a trainable ViT-adapter [32], allowing specialization for embodiment-aware traversability prediction without full fine-tuning. The robot state vector $s_t \in \mathbb{R}^6$ is processed by an MLP to produce FiLM parameters (γ_t, β_t) [33], which modulate the ViT feature map \mathbf{F} via

$$\tilde{\mathbf{F}} = \mathbf{F} \odot (1 + \gamma_t) + \beta_t. \quad (10)$$

This modulation injects embodiment-specific constraints into the visual representation.

The FiLM-adapted tokens are refined by a lightweight convolutional head and decoded into a dense 64×64 traversability map \hat{T}_t . Two bilinear upsampling stages expand the ViT grid from 14×14 , followed by a 1×1 convolution producing a single-channel estimate. This compact decoder preserves spatial precision and ensures that identical scenes yield embodiment-consistent traversability predictions.

4) *Diffusion policy*: Our trajectory generator is a conditional UNet f_θ following the standard downsampling–bottleneck–upsampling design [34]. At denoising step t , the network predicts the diffusion noise $\hat{\varepsilon}_t$ from the noisy trajectory sample x_t , spatial conditioning maps S_g and \hat{T}_t , and FiLM-modulated embodiment tokens Z_{film} .

a) *Spatial conditioning*: At each UNet resolution, we concatenate the noisy trajectory and conditioning maps:

$$C = [x_t, S_g, \hat{T}_t] \in \mathbb{R}^{4 \times H' \times W'}, \quad (11)$$

providing geometric and traversability guidance throughout denoising.

b) *FiLM-based token conditioning*: In parallel, FiLM-modulated tokens $Z_{\text{film}} \in \mathbb{R}^{N \times D}$ are supplied to the UNet’s cross-attention layers, following the *UNet2DConditionModel*. These tokens embed embodiment priors directly into the attention mechanism.

c) *Noise prediction*: The UNet predicts the injected noise as

$$\hat{\varepsilon}_t = f_\theta(C, t, Z_{\text{film}}), \quad (12)$$

trained with the standard DDPM objective:

$$\mathcal{L}_{\text{DDPM}} = \|\hat{\varepsilon}_t - \varepsilon\|_2^2, \quad \varepsilon \sim \mathcal{N}(0, I). \quad (13)$$

d) *Reverse diffusion*: The reverse process follows the DDPM scheduler [34], with noise levels $\{\beta_t\}_{t=1}^T$ and $\alpha_t = \prod_{i=1}^t (1 - \beta_i)$:

$$x_{t-1} = \frac{1}{\sqrt{\alpha_t}} \left(x_t - \frac{\beta_t}{\sqrt{1 - \alpha_t}} \hat{\varepsilon}_t \right) + \sigma_t z, \quad z \sim \mathcal{N}(0, I). \quad (14)$$

We adopt a cosine noise schedule for stable early denoising and consistent final predictions. During inference, trajectories are generated by iterating from $x_T \sim \mathcal{N}(0, I)$ with spatial conditioning (S_g, \hat{T}_t) and token conditioning Z_{film} applied at every block:

$$x_{t-1} = D_\theta(x_t, S_g, \hat{T}_t, Z_{\text{film}}), \quad (15)$$

until a clean trajectory heatmap x_0 is obtained, consistent with the scene geometry, traversability, and robot embodiment.

B. Learning Objectives

Let the predicted trajectory heatmap be

$$x_0 \in [0, 1]^{H \times W}, \quad (16)$$

the noisy diffusion state at timestep t be x_t , the normalized traversability map be $\hat{T} \in [0, 1]^{H \times W}$, and the start–goal tensor be S_g . Start and goal coordinates extracted from S_g are denoted \mathbf{s} and \mathbf{g} , respectively.

1) *Directional Forward–Flow Loss*: We encourage the predicted trajectory in (16) to follow the direction from start to goal. The unit direction vector is

$$\mathbf{d} = \frac{\mathbf{g} - \mathbf{s}}{\|\mathbf{g} - \mathbf{s}\|_2} = (d_x, d_y). \quad (17)$$

Let $\partial_x x_0$ and $\partial_y x_0$ denote Sobel spatial gradients. The directional derivative is

$$D(u, v) = \partial_x x_0(u, v) d_x + \partial_y x_0(u, v) d_y. \quad (18)$$

Backward flow (negative projection onto \mathbf{d}) is penalized:

$$\mathcal{L}_{\text{dir}} = \frac{1}{HW} \sum_{u,v} \max(0, -D(u, v)) x_0(u, v). \quad (19)$$

2) *Path probability distribution*: Given raw trajectory logits x , we define a spatial distribution via a global softmax:

$$p(u, v) = \frac{\exp(x(u, v)/T)}{\sum_{i,j} \exp(x(i, j)/T)}. \quad (20)$$

This distribution is used for all mass-based objectives.

3) *Traversability expectation reward*: The expected traversability under the distribution in (20) is

$$\mathbb{E}_p[\hat{T}] = \sum_{u,v} p(u, v) \hat{T}(u, v). \quad (21)$$

We encourage high-traversability solutions:

$$\mathcal{L}_{\text{trav}} = 1 - \max_b \mathbb{E}_{p_b}[\hat{T}_b]. \quad (22)$$

4) *Mass-based regularization*: To ensure geometric plausibility, we aggregate penalties for (i) probability near obstacles, (ii) local path thickness, (iii) entropy compactness, and (iv) spatial smoothness into a single regularizer:

$$\mathcal{L}_{\text{mass}} = \frac{1}{HW} \sum_{u,v} p(u, v). \quad (23)$$

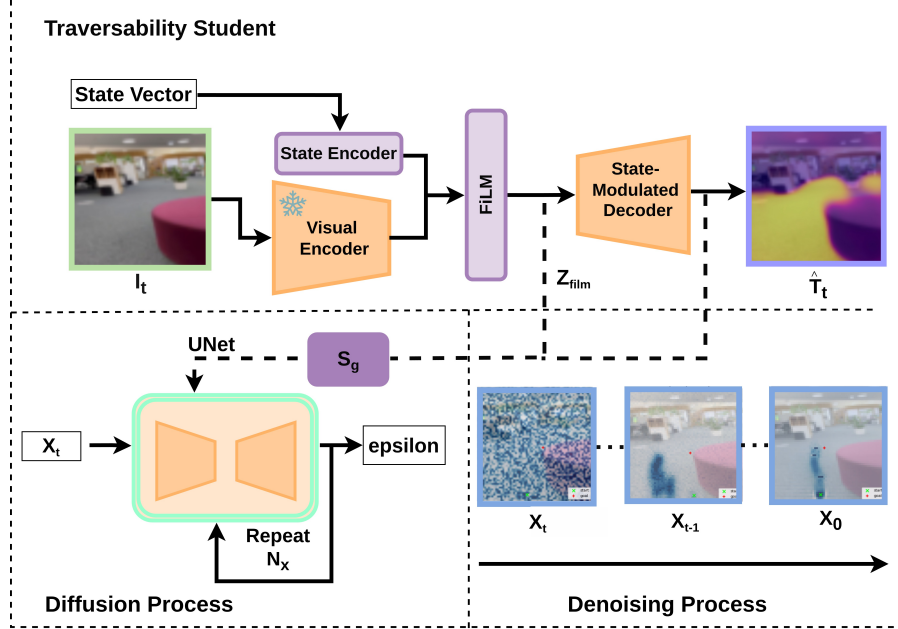


Fig. 2. The proposed model consists of two interconnected components: (1) *Traversability Student model*, where a frozen visual encoder and state encoder jointly modulate features via FiLM to produce a traversability prediction distilled from a vision–language model (VLM); and (2) *Diffusion-based Trajectory Generation*, where the UNet progressively denoises a random trajectory x_t conditioned on the modulated visual features and start–goal vector, yielding feasible and safe paths x_0 . The process repeats for N denoising steps.

5) *Traversability distillation Loss*: To train the student traversability head, we distill supervision from the teacher map $T \in [0, 1]^{H \times W}$. The student prediction \hat{T} is encouraged to match the teacher using an ℓ_1 regression loss:

$$\mathcal{L}_{\text{distil}} = \frac{1}{HW} \sum_{u,v} \left| \hat{T}(u,v) - T(u,v) \right|. \quad (24)$$

6) *Denoising Loss*: The diffusion model predicts noise $\hat{\varepsilon}_t$ and is trained with

$$\mathcal{L}_{\text{noise}} = \|\hat{\varepsilon}_t - \varepsilon\|_2^2. \quad (25)$$

7) *Final objective*: The complete training loss combines all components:

$$\mathcal{L} = \mathcal{L}_{\text{noise}} + \mathcal{L}_{\text{dir}} + \mathcal{L}_{\text{trav}} + \mathcal{L}_{\text{mass}} + \mathcal{L}_{\text{distil}}. \quad (26)$$

V. EXPERIMENTS AND RESULTS

A. UAV Simulation

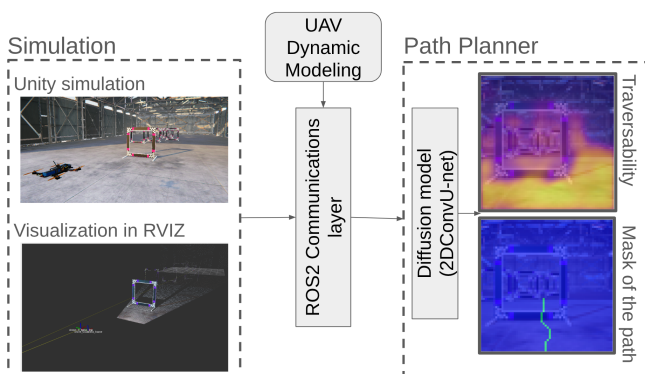


Fig. 3. UAV simulation architecture.

For this work, we developed a simulated environment. An overview of the system is shown in Fig. 3. Following the design principles of Flightmare [35], we decoupled the Unity-based visual simulator from the dynamic quadcopter model. The dynamic model and the controller are run on a separate ROS node, which sends the quadcopter state to the Unity simulator.

Given the quadcopter state, Unity computes the RGB image, depth image, and point cloud. The RGB image is then provided to the diffusion pipeline (described in the following sections) to generate a mask of the path. This mask is projected onto the point cloud to extract the points corresponding to the path. Finally, the resulting path is sent back to the dynamic model node for path-following control. The same approach to 3D path extraction is also applied in real-world experiments.

B. UAV Setup

The UAV platform is an 8-inch custom quadrotor equipped with a SpeedyBee F405 flight controller running ArduPilot. High-level control and communication with the flight stack are handled through MAVROS. While trajectory generation is executed off-board, an onboard Intel NUC performs local computation for state estimation and real-time control. Vehicle pose is provided by OpenVINS [36], which fuses visual data from the Intel RealSense T265 with inertial measurements to produce robust visual–inertial odometry. All components operate within the ROS ecosystem, ensuring unified message passing and seamless integration across perception, state estimation, and control modules.

C. Quadruped Robot Setup

The ground robot platform consists of a Unitree Go1 robot. For perception, an Intel RealSense D435i camera is front-mounted, providing a stereo RGB stream at 15Hz for model inference and a synchronized metric point cloud used exclusively for projecting the planned path into the robot's egocentric frame. For model onboard inference and sensor processing an Nvidia Jetson Orin AGX is mounted on its back, which is also used to communicate with the robot SDK where velocity controller commands are sent for tracking the path obtained from the model inference.

For evaluation, we use a VICON motion-capture system to obtain millimeter-accurate pose estimates for both the UAV and quadruped. This external tracking enables precise metric computation in a consistent world frame, independent of onboard odometry. For inference, an off-board workstation with an NVIDIA RTX 4090 is used; our model remains lightweight, requiring no more than 4GB of GPU memory.

D. Dataset Generation

Our dataset contains synchronized RGB, and depth, streams from an Intel RealSense D435i mounted on a Unitree Go1 and a custom aerial robot. For each RGB frame, we automatically generate a synthetic training trajectory without human annotation or planning. The start point is sampled near the lower image border, the goal is selected in a distant high-traversability region predicted by the teacher model, and intermediate points are formed using randomized Bézier curves to create diverse but coherent paths. The state vectors were extracted from visual odometry.

We collect 4000 images per embodiment (Go1 and UAV), yielding 8000 self-supervised samples with paired synthetic trajectories. During training, these trajectories act as soft supervisory signals whose variability is stabilized through the diffusion prior and multi-modal conditioning on visual, state, and traversability inputs. This design enables the model to learn consistent cross-embodiment motion priors without explicit geometric planning or manual labels.

E. Baselines

To the best of our knowledge, no existing method jointly learns VLM-conditioned traversability together with diffusion-based trajectory generation across multiple embodiments. Consequently, we implement our own baseline model that is conditioned only on traversability maps and start-goal heatmaps, following the same conditioning structure as our proposed method, but without incorporating the robot state vector or the traversability semantics at the feature level. The traversability maps used for this baseline are generated using [5] using the dataset described in the previous section. This baseline is inspired by [37] and employs a 1D UNet backbone for trajectory prediction. During sampling, the baseline model inpaints masked regions corresponding to the start and goal locations, while expert trajectories obtained from an A* planner provide supervision for generating feasible paths conditioned

on the traversability map and endpoint positions in image space. For the drone embodiment, the baseline is trained on 11,500 expert trajectories, whereas a mixed dataset of 9,000 trajectories (balanced between drone and quadruped) is used in the multi-embodiment setting. These trajectories are obtained by annotating multiple start points for the same goal on each image.

The model employs a ResNet-18 encoder adapted for single-channel input to process the traversability map, together with a two-layer MLP that embeds the normalized start and goal coordinates. A cosine noise schedule is used to stabilize the DDPM training procedure.

The final loss combines a trajectory reconstruction term and a start/goal-specific consistency term. The overall objective is given in (29):

$$\mathcal{L}_{\text{total}} = \lambda_{\text{dist}} \mathcal{L}_{\text{path_dis}} + \lambda_{\text{last}} \mathcal{L}_{\text{last}}, \quad (27)$$

where λ_{dist} and λ_{last} are weighting coefficients.

The trajectory reconstruction loss (28) penalizes pixel-wise deviations between predicted and ground-truth trajectory masks:

$$\mathcal{L}_{\text{path_dis}} = \frac{1}{B|\Omega|} \sum_{b,(u,v)} (\hat{\tau}_b(u,v) - \tau_b(u,v))^2, \quad (28)$$

where B is the batch size and Ω the set of all pixel coordinates.

The start/goal reconstruction loss (29) enforces accuracy on the endpoint heatmaps:

$$\mathcal{L}_{\text{total}} = \lambda_{\text{dist}} \mathcal{L}_{\text{path_dis}} + \lambda_{\text{last}} \mathcal{L}_{\text{last}} \quad (29)$$

where \hat{S}_b, \hat{G}_b denote predicted start and goal masks, and S_b, G_b their ground truth.

This baseline setup allows us to evaluate how essential platform-specific context is for achieving embodiment-generalizable behavior, and whether high-quality initial trajectories can be learned without relying on extensive planner-generated datasets—whose creation is often costly and time-consuming.

F. Ablation Metrics

Our objective is reliable, embodiment-aware traversability rather than globally optimal paths. Thus, evaluation emphasizes feasibility and safety—using clearance, cost, and success rate, while path length and latency are reported for completeness. We compute all metrics directly from the generated trajectory $\tau = \{p_1, \dots, p_N\}$ and the predicted traversability map \hat{T} , using the ground-truth traversability map T as reference. Let \mathcal{G} denote the goal region, \mathcal{O} the obstacle set, and $C(x)$ the teacher-derived traversability cost.

a) Image path metrics.: Trajectory length is evaluated as the cumulative Euclidean distance between successive trajectory points, as defined in:

$$\text{Length} = \sum_{i=1}^{N-1} \|p_{i+1} - p_i\|_2. \quad (30)$$

Clearance is computed as the average distance from each trajectory point to the closest obstacle, following:

$$\text{Clearance} = \frac{1}{N} \sum_{i=1}^N \min_{o \in \mathcal{O}} \|p_i - o\|_2. \quad (31)$$

To quantify how often the trajectory passes through low-traversability regions, we compute the normalized cost along the path using:

$$\text{Cost} = \frac{1}{N} \sum_{i=1}^N C(p_i) \cdot 100\%. \quad (32)$$

Finally, inference latency is averaged over K runs, as defined in:

$$\text{Latency} = \frac{1}{K} \sum_{k=1}^K t_k^{(\text{inf})}. \quad (33)$$

G. Ablation Studies

All ablation studies are performed on a held-out validation split with unseen environments, and the best configuration is subsequently used for all real-robot and simulation deployments, ensuring no test-set leakage.

We use the quadruped robot for ablations and the aerial robot as the primary real-world platform. The quadruped dataset provides the largest and most diverse set of scenes, making it ideal for isolating architectural choices. The drone, in contrast, represents a more challenging deployment setting highly sensitive to narrow indoor structures and viewpoint-dependent traversability, thus offering a stronger test of generalization and safety. This combination provides both controlled analysis (quadruped) and demanding real-world validation (drone).

1) *Ablation: architecture components*: The ablation study evaluates how individual components of the framework affect path quality, safety, and efficiency. The full model delivers the strongest performance, producing the safest, shortest, and most coherent trajectories with the lowest inference latency.

Removing the traversability input results in a substantial drop in clearance and an increase in path cost, indicating that explicit traversability cues are essential for avoiding unsafe regions. Excluding the start-goal tensor s_g degrades directional structure, leading to longer and less consistent paths. Disabling state-conditioned FiLM modulation yields the weakest overall performance lower clearance, higher cost, and reduced safety, showing that embodiment-aware conditioning is necessary for generating physically feasible trajectories.

Overall, all components contribute positively, with traversability input, start-goal encoding, and FiLM-based visual modulation emerging as the most critical for safe and embodiment-consistent trajectory generation.

2) *Ablation: conditional architecture*: The ablation in Table II shows that *classifier-free guidance* (CFG) provides no measurable benefit for state-conditioned trajectory generation in our framework. Unlike text-to-image diffusion, where CFG amplifies weak global prompts, our model is already driven by strong, spatially aligned conditioning signals: the start-goal heatmap, the traversability prior, FiLM-modulated state

features, and ViT-derived image tokens. Consequently, the conditional and unconditional denoising predictions remain nearly identical, and their combination produces trajectories that are statistically indistinguishable from those obtained using purely conditional inference. Moreover, CFG doubles the number of U-Net evaluations per denoising step, increasing inference latency and slightly degrading path quality. For these reasons, we adopt *conditional traversability guidance* as the default choice, as it offers the best balance between accuracy and computational efficiency.

3) *Ablation: Denoising Process*: Table III evaluates how the number of diffusion denoising steps affects inference latency and trajectory quality. A clear trade-off emerges between computational cost and path accuracy. A single denoising step achieves very low latency (0.02 s) but yields trajectories with poor clearance and safety, indicating insufficient refinement of the initial sample. Increasing to 10 steps improves stability, yet the resulting paths remain noisy and geometrically suboptimal. The best performance is obtained with **20 denoising steps**, which provides the highest clearance, lowest cost, and strong safety guarantees, while keeping inference time low (0.09 s), making it suitable for real-time control. Beyond 20 steps (e.g., 50–100), we observe diminishing returns: trajectory quality plateaus or slightly degrades, while latency increases significantly. All experiments therefore use 20 diffusion steps as the default setting.

4) *Ablation: Noise Prediction vs. Sample Prediction*: In our formulation, diffusion operates directly in the *trajectory heatmap space*, where supervision consists of extremely sparse, one-pixel curves generated through Gaussian sampling and Bézier interpolation. These synthetic trajectories are approximate and non-unique, making the mapping to x_0 highly multimodal. Regressing x_0 with MSE forces the model to average over multiple plausible paths, producing blurred or unstable outputs. In contrast, predicting the diffusion noise ε aligns with the standard DDPM objective and provides a smooth, well-conditioned target at every timestep. This avoids the sparsity and multimodality problems of x_0 regression, enabling the denoiser to learn robust conditional distributions rather than brittle geometric contours. Empirically, within our state-conditioned trajectory UNet, noise prediction yields more stable optimization, faster convergence, and higher-quality trajectories, requiring fewer denoising steps for comparable accuracy (Table IV). Thus, although the goal is to produce sharp, physically feasible trajectories, the most reliable training strategy is to predict the injected noise rather than the clean heatmap. Noise prediction is therefore both the theoretically sound DDPM formulation and the empirically superior choice for trajectory generation under sparse and structurally ambiguous supervision.

H. Comparison with Baseline

1) *Qualitative comparison*: Figure 4 shows that our model produces safe, forward-directed, and obstacle-aware trajectories that closely resemble the behavior of the supervised baseline, despite never being trained on any ground-truth trajectory annotations. Our method learns trajectory structure purely from randomized synthetic curves combined with

TABLE I
EFFECT OF EACH NETWORK COMPONENT ON OVERALL PERFORMANCE.

Variant	Configuration (\checkmark = enabled)						Path (simulation)					
	Effort (Mass)	Trav. loss	Trav. input	Goal-Start (s_g)	s_g loss	Cond. vis. emb.	Len. (m) \downarrow	Clear. (pixels) \uparrow	Cost \downarrow	Lat. (s) \downarrow	Safety _{min} \uparrow	
Full model (ours)	\checkmark	\checkmark	\checkmark	\checkmark	\checkmark	\checkmark	36.31	11.36	2.88	0.09	0.96	0.98
No trav. input	\checkmark	\checkmark	\times	\checkmark	\checkmark	\checkmark	36.31	8.37	3.42	0.09	0.93	0.98
No s_g (goal-start) input	\checkmark	\checkmark	\checkmark	\times	\checkmark	\checkmark	25.00	11.26	3.37	0.09	0.95	0.98
No cond. (test)	\checkmark	\checkmark	\checkmark	\checkmark	\checkmark	\times	36.48	5.83	5.34	0.09	0.90	0.97

TABLE II
COMPARISON OF GUIDANCE STRATEGIES.

Guidance method	Len. (m) \downarrow	Clear. (pixels) \uparrow	Cost \downarrow	Lat. (s) \downarrow	Safety _{min} \uparrow	Safety _{max} \uparrow
Cond. traversability	36.31	11.36	2.88	0.09	0.96	0.98
Classification-free guidance	30.00	5.20	5.43	0.48	0.96	0.98

TABLE III
EFFECT OF THE NUMBER OF DENOISING STEPS ON INFERENCE LATENCY AND TRAJECTORY QUALITY.

Steps	Lat. (s) \downarrow	Len \downarrow	Clear. (pixels) \uparrow	Cost \downarrow	Safety _{min} \uparrow	Safety _{max} \uparrow
1	0.02	33.00	2.75	5.74	0.10	0.99
10	0.05	36.48	2.75	5.88	0.89	0.97
20	0.09	36.31	11.36	2.88	0.96	0.98
50	0.20	36.31	5.40	5.74	0.83	0.86
100	0.38	36.31	4.60	6.20	0.88	0.91

TABLE IV
COMPARISON OF GENERATIVE FORMULATIONS FOR TRAJECTORY DIFFUSION. ALL RESULTS REPORTED ON SIMULATED PATHS.

Generative model	Len. (m) \downarrow	Clear. (pixels) \uparrow	Cost \downarrow	Lat. (s) \downarrow	Safety _{min} \uparrow	Safety _{max} \uparrow
DDPM (ϵ-prediction) + UNet	36.31	11.36	2.88	0.09	0.96	0.98
DDPM (sample-prediction)+ UNet	35.00	2.95	5.66	0.09	0.73	0.99

traversability-driven regularization, yet consistently returns compact and feasible paths aligned with the robot's embodiment.

To ensure fair evaluation, the baseline was only tested under the 50% training data regime, as using 30% would introduce severe class imbalance due to its complete reliance on dense, supervised trajectory annotations and lack of cross-embodiment priors. Our method maintains strong performance even at 30% data precisely because it does not rely on these curated annotations. Under the 50% setting, the baseline exhibited degraded path quality, including frequent drifts into low-traversability regions. In contrast, our diffusion model maintained coherent, safe, and embodiment-consistent behavior. The baseline's inability to encode embodiment-specific feasibility prevents knowledge transfer across different robot bodies. These results validate that our planner-free, annotation-free framework produces high-quality, embodiment-conditioned trajectories that remain competitive with supervised baselines, even when data is limited.

a) Quantitative comparison: The comparison reveals clear practical differences between the two approaches. The baseline achieves lower MSE due to pixel-aligned supervision, but requires a 100-step diffusion process, resulting in much

higher inference latency. In contrast, our model uses only 20 steps and generates trajectories in 0.09 s, making it genuinely real-time.

Despite the higher MSE from synthetic, non-aligned supervision, our approach consistently achieves superior safety and clearance, producing paths with greater free-space margins and higher minimum traversability.

Overall, Table V shows that although the baseline benefits from full supervision, our approach offers a more efficient and safety-aware alternative, achieving real-time performance and strong generalization without perfect trajectory annotations or long diffusion chains.

I. Simulation Deployment

In simulation, we conducted a more extensive evaluation focused on a single aerial agent by testing across five progressively more challenging obstacle configurations. These scenarios included narrow passages, multi-gate sequences, cluttered indoor structures, and layouts containing distractor obstacles absent from the training set. This suite of environments was intentionally designed to stress-test the model's robustness and probe its ability to generate safe trajectories under significant geometric variation.

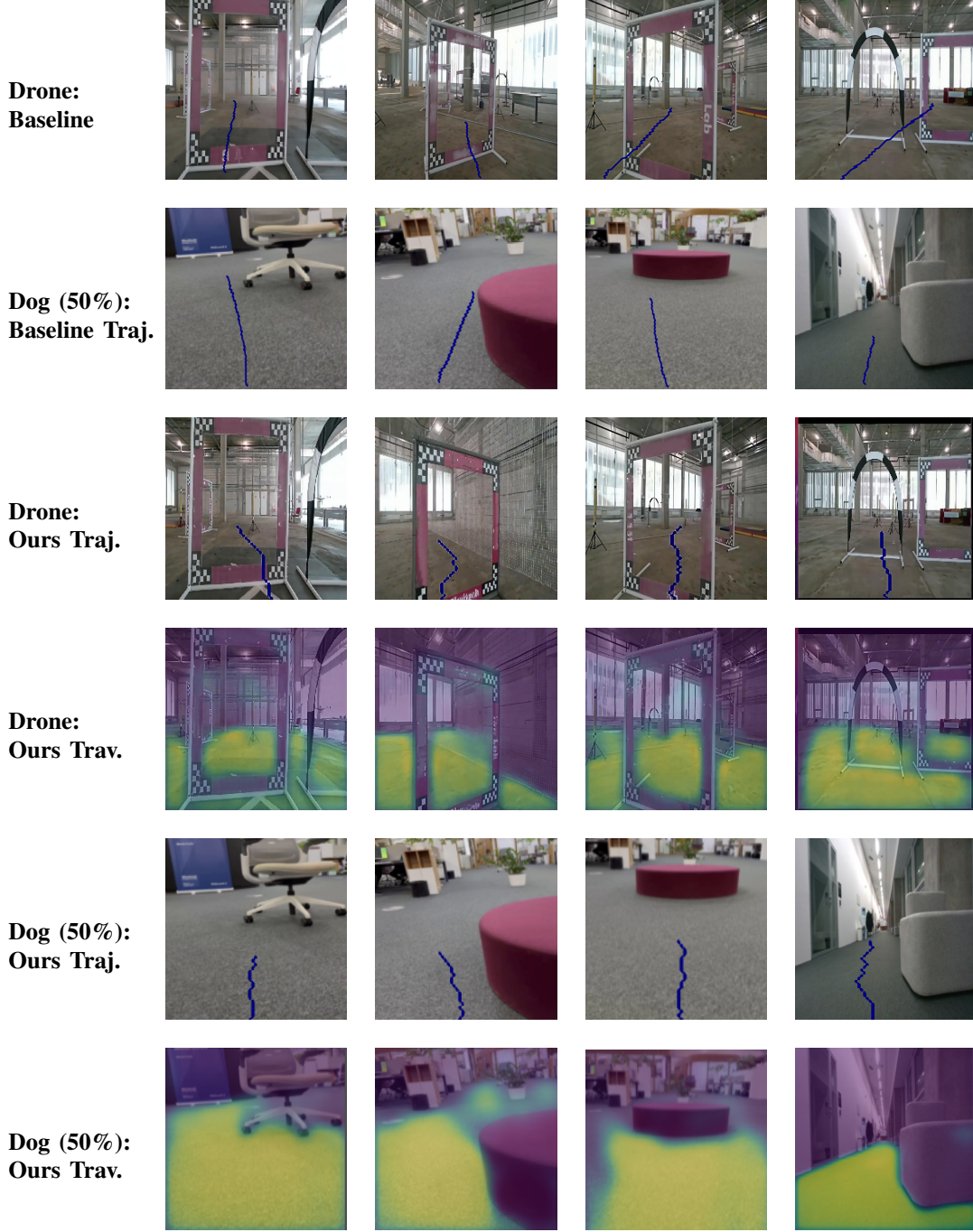


Fig. 4. Qualitative comparison between baseline and our method across drone and quadruped platforms. Rows show (i) baseline trajectories, (ii) baseline traversability, (iii) our trajectories, and (iv) our predicted traversability maps. Our model exhibits smoother, safer, and embodiment-aware path generation.

Crucially, the model was never trained on any simulation data all learning was based solely on real-world RGB observations and traversability cues. Despite this, the policy consistently produced collision-free, physically plausible trajectories across most configurations, achieving an overall success rate of 80% (Table VI). This demonstrates that our joint traversability–trajectory formulation captures generalizable motion priors that transfer effectively to novel, synthetic layouts without any domain adaptation, prompt engineering, or retraining.

J. Real-world experiments

Our real-world experiments are designed to evaluate the proposed framework across heterogeneous platforms (legged robot and aerial robot) under several deployment-oriented objectives:

- 1) **Embodiment-Aware Feasibility.** Evaluates whether generated trajectories remain physically valid and safe for each platform (ground-constrained motion for the quadruped and free-space navigation for the drone).
- 2) **Training-Data Efficiency.** Measures performance un-

TABLE V
TRAJECTORY RECONSTRUCTION, LATENCY, AND SAFETY COMPARISON BETWEEN THE BASELINE AND OUR MODEL ACROSS TWO DATASET SETTINGS.

Setting	MSE \downarrow	Lat. (s) \downarrow	Clear. (px) \uparrow	Safety _{min} \uparrow	Safety _{max} \uparrow
Baseline					
Drone (100%)	0.018	0.24	4.85	0.26	0.69
Dog (50%)	0.015	0.24	8.67	0.55	0.83
Ours					
Drone (100%)	0.045	0.09	8.75	0.50	0.80
Dog (50%)	0.130	0.09	10.45	0.72	0.85

TABLE VI
SIMULATION DRONE EVALUATION USING DRONE DATA.

Robot	Data (%)	Run	Path Len. (m) \downarrow	Min. Clear. (m) \uparrow	Planner Len. (m) \downarrow	Avg. Time (s) \downarrow
Drone	100	1	39.50	0.41	39.36	39.42
		2	37.69	0.30	38.47	39.60
		3	38.22	0.44	37.89	36.94
		4	35.19	0.37	38.79	33.15
		5	40.22	0.11	39.07	39.97
Success Rate			80%			

der reduced embodiment-specific data. We test the quadruped with limited training fractions and the drone under 50% and 70% regimes to assess sensitivity to reduced supervision.

3) **Cross-Scene Generalization.** Assesses how well the drone model (trained with 100% of its data) transfers to three unseen indoor layouts with different geometric structures.

For every run we measure: (i) predicted path length, (ii) minimum obstacle clearance obtained from the point cloud obtained from realsense camera, (iii) planner baseline length, (iv) execution time, and (v) binary success indicating whether the robot completed the route without collision or operator intervention. A trial is considered successful if the robot reaches the goal safely and without human correction.

To increase the safety margin around obstacles, a repulsive force was applied to all trajectory points. This force shifts any point that is too close to an obstacle in the direction of the separation velocity v_s , ensuring that the trajectory remains collision-free. The separation velocity v_s considers all point-cloud points within a sphere of a specified minimum radius and is computed as:

$$v_s = -c_s \sum_{k=0}^j (p_k - \tau_i), \quad (34)$$

where p_k is the position of the k -th point in the point cloud located inside the sphere, τ_i is the position of the i -th trajectory point, and c_s is a scaling coefficient.

1) **Cross-scene generalization:** We primarily conduct experiments on the aerial robot, focusing on evaluating its ability to generalize to unseen indoor environments. We have chosen three unseen indoor environments: (i) a single-gate setup, (ii) two gates placed sequentially, and (iii) a gate followed by an unseen obstacle. As shown in Table VIII, the drone achieves

high success rates both in environments similar to the training distribution and in settings with newly introduced obstacles. A slight performance drop occurs in the two-gate scenario, which presents a more cluttered layout with narrow passages, making navigation inherently more challenging.

Importantly, we find that *small, post-hoc modifications* to the traversability map such as applying a cone-shaped visibility mask around the drone's forward direction can further guide the trajectory without *any* model retraining. This demonstrates that the diffusion model remains highly steerable at inference time: low-level geometric constraints can be injected directly through the traversability map to influence the final trajectory, preserving safety while improving path shaping when required.

2) **Cross-embodiment robot experiments:** We evaluate the proposed model on a real robot dog using four training regimes: 100%, 50%, and 30% in the same unseen indoor scenario. Each trained model is deployed over three navigation trials in a cluttered and narrow environment. Furthermore, we show that introducing a new embodiment during training does not significantly degrade the performance of the primary agent, indicating strong cross-embodiment transfer.

a) **High-data regime (100% and 50%).** The models trained with full data and with only half of the data both achieve a **100% success rate**. Table VII shows that even at 50%, the predicted paths maintain high clearance (0.26–0.67 m), remain comparable in length to planned trajectory, and execute reliably in all trials. This demonstrates strong embodiment-specific learning and robust generalization to real indoor environments.

b) **Moderate-data regime (30%).** With 30% of the training data, the success rate drops to **67%**. Nevertheless, two of the three trials still succeed with reasonable path lengths, and the single failure is attributed to a borderline clearance of just 0.19m. Importantly, even in this highly data-limited regime, the model continues to generate coherent and feasible

TABLE VII
ROBOT DOG EVALUATION ACROSS DIFFERENT TRAINING DATA FRACTIONS.

Robot	Data (%)	Run	Path Len. (m)↓	Min. Clear. (m)↑	Planner Len (m)↓	Avg. Time (s)↓	Success↑
100	100	1	14.42	1.67	9.34	123	1
		2	8.26	0.67	8.21	66	1
		3	9.35	1.24	11.34	76	1
Success Rate							100%
Dog	50	1	11.23	0.34	10.90	89	1
		2	11.63	0.26	10.35	68	1
		3	7.90	0.62	11.50	66	1
Success Rate							100%
30	30	1	7.81	0.48	13.12	59	1
		2	4.70	1.00	10.34	55	1
		3	9.56	0.19	11.53	92	0
Success Rate							67%
70	70	1	8.37	0.4	8.42	35.47	1
		2	7.15	0.38	8.48	31.81	1
		3	3.86	0.13	4.99	18.21	0
Success Rate							67%

TABLE VIII
QUADCOPTER EVALUATION IN DIFFERENT OBSTACLE CONFIGURATIONS.

Configuration	Run	Path Len. (m)↓	Min. Clear. (m)↑	Planner Len. (m)↓	Avg. Time (s)↓	Success↑
Gate	1	7.40	0.51	7.96	35.15	1
	2	6.88	0.44	9.35	30.40	1
	3	7.06	0.41	9.25	30.80	1
Success Rate						100%
Gate + Obstacle	1	7.06	0.53	7.98	31.88	1
	2	7.03	0.29	7.45	31.65	1
	3	6.76	0.38	8.32	34.02	1
Success Rate						100%
Two Gates	1	7.19	0.49	9.34	33.40	1
	2	7.20	0.34	10.73	31.12	1
	3	6.79	0.09	8.50	31.09	0
Success Rate						67%

trajectories, its occasional unsafe shortcuts stem from the reduced diversity rather than systematic failure. A comparable performance drop is observed for the main aerial agent under the same 30% data setting, further confirming that the degradation is due to limited training data rather than embodiment-specific weakness.

VI. CONCLUSION

We introduced a unified diffusion framework that predicts traversability and generates feasible, embodiment-aware trajectories directly from a single RGB image. A key result is that perfect trajectory supervision is unnecessary: randomized, planner-free trajectory sampling combined with targeted regularization provides sufficient structure for learning safe and stable motion without demonstrations or expert planners.

By jointly learning traversability and trajectory denoising, the model infers embodiment-specific feasible regions from

only a compact state vector, enabling efficient conditioning with modest data and allowing the same architecture to generalize across heterogeneous robot platforms. Moreover, SwarmDiffusion’s lightweight design supports rapid adaptation to new embodiments, requiring only limited additional visual and state information.

Experiments on an aerial robot and a quadruped demonstrate 80–100% navigation success, strong clearance margins, real-time inference, and reliable generalization to unseen environments—even when adapting to a new robot with minimal additional data. The method consistently outperforms a supervised baseline that lacks embodiment-aware traversability reasoning.

Overall, the results show that prompt-free, planner-free, and annotation-free trajectory generation is both feasible and effective. Integrating traversability estimation with diffusion-based path synthesis establishes a scalable foundation for future research, including multi-step and long-horizon planning,

richer 3D geometric reasoning, multi-robot coordination, and autonomous exploration guided by generalizable traversability priors. Looking forward, the same paradigm may extend beyond navigation, offering a unified mechanism for guiding action generation in broader embodied AI tasks.

REFERENCES

- [1] D. A. Gómez-Rosal, M. Bergau, G. K. Fischer, A. Wachaja, J. Grater, M. Odenweller, U. Piechottka, F. Hoeflinger, N. Gosala, N. Wetzel, D. Buetscher, A. Valada, and W. Burgard, “A smart robotic system for industrial plant supervision,” in *2023 IEEE SENSORS*, pp. 1–4, 2023.
- [2] K. Weerakoon, A. J. Sathyamoorthy, M. Elnoor, and D. Manocha, “Adventr: Autonomous robot navigation in complex outdoor environments,” in *International Symposium on Experimental Robotics*, pp. 219–228, Springer, 2023.
- [3] J. Frey, M. Mattamala, N. Chebrolu, C. Cadena, M. Fallon, and M. Hutter, “Fast Traversability Estimation for Wild Visual Navigation,” in *Proceedings of Robotics: Science and Systems*, (Daegu, Republic of Korea), July 2023.
- [4] M. V. Gasparino, A. N. Sivakumar, and G. Chowdhary, “Wayfaster: a self-supervised traversability prediction for increased navigation awareness,” in *Proc. IEEE Int. Conf. on Rob. and Auto.*, pp. 8486–8492, IEEE, 2024.
- [5] S. Sahu, A. Singh, K. Nambiar, S. Saripalli, and P. Sujit, “Anytraverse: An off-road traversability framework with vlm and human operator in the loop,” *arXiv preprint arXiv:2506.16826*, 2025.
- [6] Z. Zhang, A. Lin, C. W. Wong, X. Chu, Q. Dou, and K. W. Samuel Au, “Interactive navigation in environments with traversable obstacles using large language and vision-language models,” in *2024 IEEE International Conference on Robotics and Automation (ICRA)*, pp. 7867–7873, 2024.
- [7] S. Jung, J. Lee, X. Meng, B. Boots, and A. Lambert, “V-strong: Visual self-supervised traversability learning for off-road navigation,” in *Proc. IEEE Int. Conf. on Rob. and Auto.*, pp. 1766–1773, 2024.
- [8] R. Julian, K. Stone, W. Koch, A. Faust, I. Gilitschenski, and J. P. How, “Badgr: Learning to drive from raw sensor data using self-supervision,” in *Proc. Rob.: Sci. and Syst.*, 2020.
- [9] E. Chen, C. Ho, M. Maulimov, C. Wang, and S. Scherer, “Learning-on-the-drive: Self-supervised adaptation of visual offroad traversability models,” 2024.
- [10] H.-S. Yoon, J.-H. Hwang, C. Kim, E. I. Son, S.-W. Yoo, and S.-W. Seo, “Adaptive robot traversability estimation based on self-supervised online continual learning in unstructured environments,” *IEEE Rob. and Auto. Let.*, vol. 9, no. 6, pp. 4902–4909, 2024.
- [11] F. A. Ruetz, N. Lawrence, E. Hernández, P. V. K. Borges, and T. Peynot, “Foresttrav: 3d lidar-only forest traversability estimation for autonomous ground vehicles,” *IEEE Access*, vol. 12, pp. 37192–37206, 2024.
- [12] J. Zurn, W. Burgard, and A. Valada, “Self-supervised visual terrain classification from unsupervised acoustic feature learning,” *IEEE Transactions on Robotics*, vol. 37, pp. 466–481, 2019.
- [13] M. Sivaprakasam, S. Triest, C. Ho, S. Aich, J. Lew, I. Adu, W. Wang, and S. Scherer, “Salon: Self-supervised adaptive learning for off-road navigation,” *arXiv preprint arXiv:2412.07826*, 2024.
- [14] T. Ran, L. Yuan, and J. Zhang, “Scene perception based visual navigation of mobile robot in indoor environment,” *ISA Transactions*, vol. 109, pp. 389–400, 2021.
- [15] F. Wang, C. Zhang, W. Zhang, C. Fang, Y. Xia, Y. Liu, and H. Dong, “Object-based reliable visual navigation for mobile robot,” *Sensors*, vol. 22, no. 6, 2022.
- [16] H. Huang, G. Zhu, Z. Fan, H. Zhai, Y. Cai, Z. Shi, Z. Dong, and Z. Hao, “Vision-based distributed multi-uav collision avoidance via deep reinforcement learning for navigation,” in *Proc. 2022 IEEE/RSJ International Conference on Intelligent Robots and Systems (IROS)*, pp. 13745–13752, 2022.
- [17] Z. Wang, S. X. Ng, and M. El-Hajjar, “Deep reinforcement learning assisted uav path planning relying on cumulative reward mode and region segmentation,” *IEEE Open Journal of Vehicular Technology*, vol. 5, pp. 737–751, 2024.
- [18] T. Liu, H. Zhong, J. Hu, and T. Zhang, “Safemove-rl: A certifiable reinforcement learning framework for dynamic motion constraints in trajectory planning,” 2025.
- [19] A. Romero, A. Shenai, I. Geles, E. Aljalbout, and D. Scaramuzza, “Dream to fly: Model-based reinforcement learning for vision-based drone flight,” 2025.
- [20] M. Stamatopoulou, J. Liu, and D. Kanoulas, “Dippest: Diffusion-based path planner for synthesizing trajectories applied on quadruped robots,” 2024.
- [21] A. Sridhar, D. Shah, C. Glossop, and S. Levine, “Nomad: Goal masked diffusion policies for navigation and exploration,” in *2024 IEEE International Conference on Robotics and Automation (ICRA)*, pp. 63–70, 2024.
- [22] J. Carvalho, A. T. Le, P. Kicki, D. Koert, and J. Peters, “Motion planning diffusion: Learning and adapting robot motion planning with diffusion models,” *IEEE Transactions on Robotics*, vol. 41, pp. 4881–4901, 2025.
- [23] A. Zhang, X. Meng, L. Calliari, D.-K. Kim, S. Omidshafiei, J. Biswas, A. Agha, and A. Shaban, “Ventura: Adapting image diffusion models for unified task conditioned navigation,” *arXiv preprint arXiv:2510.01388*, 2025.
- [24] Y. Zeng, H. Ren, S. Wang, J. Huang, and H. Cheng, “Navidiffusor: Cost-guided diffusion model for visual navigation,” in *2025 IEEE International Conference on Robotics and Automation (ICRA)*, pp. 11994–12001, 2025.
- [25] V. Serpiva, A. Lykov, F. Batool, V. Kozlovskiy, M. A. Cabrera, and D. Tsetserukou, “Flightdiffusion: Revolutionising autonomous drone training with diffusion models generating fpv video,” 2025.
- [26] X. Wang, Y. R. Tan, W. Leong, S. Huang, R. Teo, and C. Xiang, “Gps denied ibvs-based navigation and collision avoidance of uav using a low-cost rgb camera,” 2025.
- [27] Z. Li, Y. Yi, Z. Niu, and N. Atanasov, “EAST: environment-aware safe tracking for robot navigation in dynamic environments,” *Autonomous Robots*, vol. 49, no. 4, p. 36, 2025.
- [28] I. Zhura, D. Davletshin, N. D. W. Mudalige, A. Fedoseev, R. Peter, and D. Tsetserukou, “Neuroswarm: Multi-agent neural 3d scene reconstruction and segmentation with uav for optimal navigation of quadruped robot,” in *2023 IEEE International Conference on Systems, Man, and Cybernetics (SMC)*, pp. 2525–2530, 2023.
- [29] X. Cao, M. Li, Y. Tao, and P. Lu, “Hma-sar: Multi-agent search and rescue for unknown located dynamic targets in completely unknown environments,” *IEEE Robotics and Automation Letters*, vol. 9, no. 6, pp. 5567–5574, 2024.
- [30] A. Zhang, X. Meng, L. Calliari, D.-K. Kim, S. Omidshafiei, J. Biswas, A. Agha, and A. Shaban, “Ventura: Adapting image diffusion models for unified task conditioned navigation,” 2025.
- [31] M. Oquab, T. Darcet, T. Moutakanni, H. V. Vo, M. Szafraniec, V. Khalidov, P. Fernandez, D. HAZIZA, F. Massa, A. El-Nouby, M. Assran, N. Ballas, W. Galuba, R. Howes, P.-Y. Huang, S.-W. Li, I. Misra, M. Rabbat, V. Sharma, G. Synnaeve, H. Xu, H. Jegou, J. Mairal, P. Labatut, A. Joulin, and P. Bojanowski, “DINOv2: Learning robust visual features without supervision,” *Transactions on Machine Learning Research*, 2024.
- [32] Z. Chen, Y. Duan, W. Wang, J. He, T. Lu, J. Dai, and Y. Qiao, “Vision transformer adapter for dense predictions,” in *Int. Conf. Learn. Represent.*, 2023.
- [33] E. Perez, F. Strub, H. De Vries, V. Dumoulin, and A. Courville, “Film: Visual reasoning with a general conditioning layer,” in *Proceedings of the AAAI conference on artificial intelligence*, vol. 32, 2018.
- [34] P. von Platen, S. Patil, A. Lozhkov, P. Cuenca, N. Lambert, K. Rasul, M. Davaadorj, D. Nair, S. Paul, W. Berman, Y. Xu, S. Liu, and T. Wolf, “Diffusers: State-of-the-art diffusion models.” <https://github.com/huggingface/diffusers>, 2022.
- [35] Y. Song, S. Naji, E. Kaufmann, A. Loquercio, and D. Scaramuzza, “Flightmare: A flexible quadrotor simulator,” in *Conference on Robot Learning*, 2020.
- [36] P. Geneva, K. Eckenhoff, W. Lee, Y. Yang, and G. Huang, “Openvins: A research platform for visual-inertial estimation,” in *2020 IEEE International Conference on Robotics and Automation (ICRA)*, pp. 4666–4672, 2020.
- [37] J. Liang, A. Payandeh, D. Song, X. Xiao, and D. Manocha, “DTG : Diffusion-based Trajectory Generation for Mapless Global Navigation,” in *2024 IEEE/RSJ International Conference on Intelligent Robots and Systems (IROS)*, pp. 5340–5347, 2024.